Pacific Northwest NATIONAL LABORATORY

PNNL-32016 Rev 0
DVZ-RPT-062 Rev 0

Evaluation of Electrical Resistivity Tomography to Monitor the Transport of Past Releases Beneath Tank Farms

September 2021

Yue Zhu
Judy Robinson
Xuehang Song
Mark Rockhold
Timothy Johnson

U.S. DEPARTMENT OF ENERGY

Prepared for the U.S. Department of Energy
under Contract DE-AC05-76RL01830

PACIFIC NORTHWEST NATIONAL LABORATORY
operated by
BATTELLE
for the
UNITED STATES DEPARTMENT OF ENERGY
under Contract DE-AC05-76RL01830

Printed in the United States of America

Available to DOE and DOE contractors from the
Office of Scientific and Technical Information,
P.O. Box 62, Oak Ridge, TN 37831-0062;
ph: (865) 576-8401
fax: (865) 576-5728
email: reports@adonis.osti.gov

Available to the public from the National Technical Information Service
5301 Shawnee Rd., Alexandria, VA 22312
ph: (800) 553-NTIS (6847)
email: orders@ntis.gov <https://www.ntis.gov/about>
Online ordering: http://www.ntis.gov

PNNL-32016 Rev 0
DVZ-RPT-062 Rev 0

Evaluation of Electrical Resistivity Tomography to Monitor the Transport of Past Releases Beneath Tank Farms

September 2021

Yue Zhu
Judy Robinson
Xuehang Song
Mark Rockhold
Timothy Johnson

Prepared for
the U.S. Department of Energy
under Contract DE-AC05-76RL01830

Pacific Northwest National Laboratory
Richland, Washington 99354

Summary

Underground storage tanks at the Hanford Site, in southeastern Washington State, hold radioactive waste generated from four decades of plutonium production. The 149 single-shell tanks and the 28 double-shell tanks have all exceeded their initial design life of approximately 25 years. At least 67 tanks are assumed to have leaked in the past, resulting in radioactive releases into the vadose zone. Gamma ray logging within dry monitoring wells is currently the primary method for tracking the migration of leaked tank waste through the vadose zone. While this approach provides an accurate assessment of radioactive contamination, that information is only provided near (within ~1m) the borehole, leaving most of the vadose zone unmonitored, particularly the important region directly beneath the tank.

This report describes a numerical study that investigates the feasibility and performance of time-lapse 3D electrical resistivity tomography (ERT) for long-term monitoring of a hypothetical tank waste location and migration through the vadose zone. ERT is a method of remotely imaging the bulk electrical conductivity (EC) of the subsurface, which is significantly impacted by the presence of conductive solid and liquid tank waste. The release of liquid tank wastes increases subsurface fluid conductivity and saturation over time, creating a target to use time-lapse ERT for long-term monitoring. Although the presence of metallic infrastructure can cause ERT interference, recent advancements in ERT data processing enable the deleterious effects of buried metallic infrastructure (e.g. pipes, wellbore casings, tanks) to be removed to better determine the liquid tank waste migration over time.

Three hypothetical realistic scenarios were simulated in the ERT evaluation. The first two scenarios assume the same leak amount and rate (i.e., between 1/1/1951 and 12/31/1951 at the rate of 347 m^3 per year) but different leaky tanks. Scenario 1 assumes leaks under tank B-102, which is located on the edge of the B-tank farm and surrounded by a few metallic infrastructure including cased pipes/wells/tanks. Scenario 2 assumes leaks under tank B-108, which is located near the center of the B-tank farm and surrounded by larger amount of metallic infrastructure than B-102. Scenario 3 assumes the same metallic infrastructure as B-102, with a more recent contaminant leak that was simulated to have occurred between 1/1/2018 and 12/31/2023 at a rate of 1.89 m^3 per year. The leak time in Scenarios 1 and 2 corresponds to a historical overfill event in 1951 and Scenario 3 corresponds to a recent found tank leak in 2019.

In each scenario, a “true” bulk EC model vs. time reflecting contaminant migration was generated. ERT data was simulated from these “true” bulk EC models and a time-lapse ERT inversion produced “imaged” bulk EC vs. time. Three electrode configurations in two, four and eight boreholes surrounding the leak tank were used in the ERT simulations in each scenario. These borehole configurations were considered logistically feasible and cost-effective for monitoring. The hypothetical ERT boreholes are assumed to have non-metallic casing. By comparing the “imaged” bulk EC with the “true” bulk EC, it was demonstrated that the three configurations of wells used (two, four, and eight wells) were able to successfully monitor the migration of tank leaks through the vadose zone, with bulk EC resolution increasing with the number of down borehole ERT arrays for all scenarios. Therefore, the use of eight boreholes to perform ERT monitoring beneath the tanks provided the best spatiotemporal information.

Figure S.1 shows the results for years 2022 and 2045 for Scenario 1, which are seventy-one years and ninety-four years after the leak. The “true” bulk EC model is compared to the ERT images (i.e. imaged bulk EC) and demonstrates the ability of vertical electrodes to provide long-term monitoring for eight-, four- and two-well electrode configurations. These results demonstrate that long-term 3D monitoring can be achieved at different resolutions, but will require the installation of arrays of vertical electrodes using direct-push methods or rotary drilling.

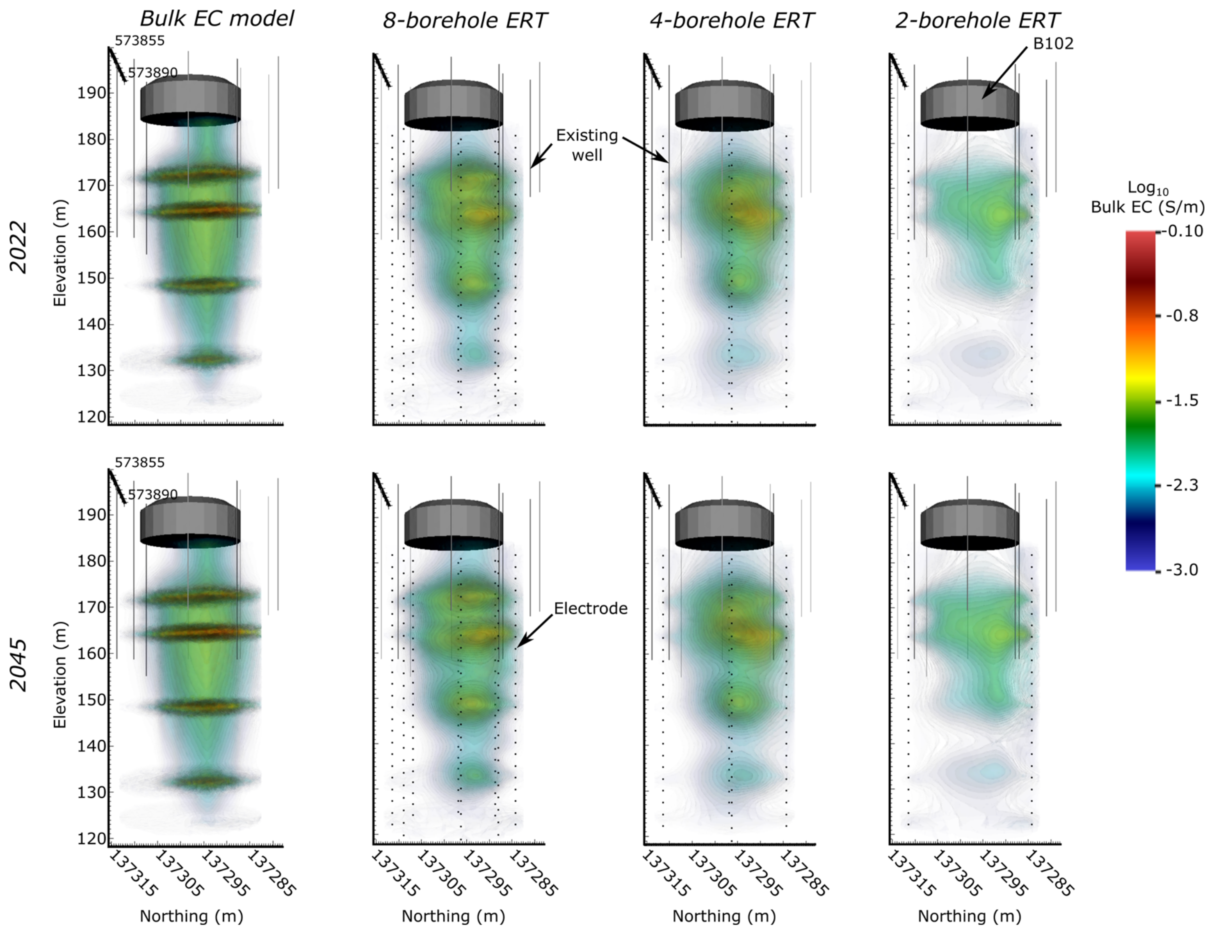

Figure S.1. Simulated bulk electrical conductivity anomalies at years 2022 and 2045 caused by a hypothetical leak under tank B-102 and corresponding ERT images using eight, four, and two vertical electrode arrays.

Acknowledgments

This document was prepared by the Deep Vadose Zone - Applied Field Research Initiative at Pacific Northwest National Laboratory. Funding for this work was provided by the U.S. Department of Energy (DOE) Richland Operations Office. The Pacific Northwest National Laboratory is operated by Battelle Memorial Institute for the DOE under Contract DE-AC05-76RL01830.

Acronyms and Abbreviations

CCU	Cold Creek unit
EC	electrical conductivity
ERT	electrical resistivity tomography
Voltage drop	ΔV
Current	I

Contents

Figures

Tables

1.0 Introduction

Underground storage tanks at the Hanford Site, in southeastern Washington State, hold radioactive waste generated from four decades of plutonium production. The 149 single-shell tanks and the 28 double-shell tanks have all exceeded their initial design life of approximately 25 years. At least 67 tanks are assumed to have leaked in the past, resulting in radioactive releases into the vadose zone (Nuclear Newswire 2021). Although the volumes of releases can be estimated, the vertical and lateral migration of tank leaks is not well characterized. Active monitoring of the migration of tank leaks toward groundwater is critical input for remediation management decisions. Current monitoring approaches rely primarily on periodic wellbore logging for radioactivity within metal-cased monitoring boreholes surrounding the tanks. However, this approach does not provide information on non-radioactive contaminants or on the distribution and migration of contaminants located at a distance from the monitoring boreholes.

Tank wastes at Hanford exhibit high ionic strength and cause an increase in bulk electrical conductivity (EC) when introduced to subsurface soils that is orders of magnitude above background levels (Johnson and Wellman 2013). Because of this, they are viable targets for electrical resistivity tomography (ERT) imaging. ERT is a method of remotely imaging the bulk EC of the subsurface. When operated in time-lapse mode, it can be used to monitor changes in subsurface bulk EC over time, which acts as a proxy for contaminant migration. ERT can potentially be used to image the 3D distribution and migration of contaminants beneath a tank farm. Once an ERT system is installed, it can be operated autonomously from data collection to processing and presentation, operating at a low cost with robust ERT systems and minimal on-site field work that can last for many decades.

Tank farms contain numerous systems of buried metallic infrastructure that normally have a deleterious influence on ERT imaging, including piping systems, monitoring wellbores, and the tanks themselves. The E4D software (https://e4d.pnnl.gov) can explicitly model the influence of metallic infrastructure as part of the ERT imaging algorithm, thereby removing its effects from the ERT images (Johnson and Wellman 2015); however, the removal of the metallic infrastructure reduces image resolution near the metal. Electrode configurations also impact optimal imaging performance. These site-specific impacts can be identified prior to executing a field campaign through a numerical modeling assessment. Hence, the objective of this work was to evaluate the feasibility and performance of ERT under different leak scenarios/metallic infractructure/electrode array configurations that can have variable degree of impact in imaging contaminants beneath tank farms.

1.1 Numerical Simulations

To assess the performance of a potential field ERT monitoring system, simulations were executed based on subsurface conditions at the B-tank farm within the B-Complex area of the Hanford Central Plateau (see Figure 2.1). This area has been of particular interest due to a recently found leak in one of the tanks (B-109) that started in 2019 (Ecology 2021).

Three hypothetical scenarios representing realistic conditions were simulated in the feasibility study. The first two scenarios assume the same leak rate and amount (leak between 1/1/1951 and 12/31/1951 at the rate of 347 m^3 per year) but different leaky tanks. Scenario 1 assumes leaks under tank B-102, which is located on the eastern side of the B-tank farm, and Scenario 2 assumes leaks under tank B-108, which is located near the center of the B-tank farm. Contaminant target in Scenario 2 was surrounded by more cased pipes/wells/tanks than Scenario 1. The two scenarios were used to assess the ERT performance under differnt influences of the metallic infrastructure. Scenario 3 assumes the same metallic infrastructure as Scenario 1 (i.e., the same leaky tank B-102) using a recent leak information (between 1/1/2018 and 12/31/2023 at a rate of 1.89 m^3 per year). The leak time in Scenarios 1 and 2 corresponds to a historical overfill event in 1951 (Serne et al. 2010) and Scneario 3 corresponds to a recent found tank leak in 2019. The geologic framework model and associated hydraulic properties for all scenarios were based on Springer (2018).

In each scenario, a “true” bulk EC model vs. time reflecting contaminant migration was generated and discretized to the ERT mesh. ERT data was simulated from these “true” bulk EC models and a time-lapse ERT inversion produced ‘imaged’ bulk EC vs. time. Three electrode configurations in two, four, and eight boreholes surrounding the leak tank were used in the ERT simulations in each scenario. The ERT boreholes are non-metallic cased, and drilling (or direct push) of new boreholes is needed. Metallic infrastructure including buried pipes, cased wells, and tanks in the B-tank farm were explicitly modeled in ERT simulations, thereby removing their effects from the ERT images. In terms of electrical current conduction, the tanks behave as metallic conductors because of dense steel reinforcement within the concrete shell and because of the steel liner on the inner boundary of the tank. The steel components of the tank are coupled to the soil through the buried concrete (National Fire Protection Association 2019).

1.2 Report Organization

This report describes ERT feasibility for the three different scenarios that differ by the quantity of subsurface metallic infrastructure and contaminant leaking parameters. Section 2.0 provides an overview of the Hanford B-tank farm. Section 3.0 discusses the basic principles of the ERT method. Conceptual models and cross-well ERT survey configurations for the different scenarios are described in Section 4.0. In Section 5.0, time-lapse ERT simulation results at early (0-20 years after leak initiated) and late (greater than 50 years after leak initiated) time stages of the contaminant leak for all scenarios are presented. Comparison of the ERT imaging results for different survey configurations are also provided. A summary of the evaluation and recommendations for applying ERT in monitoring tank farm leaks is provided in Section 6.0.

2.0 Site Description

A map of the key facilities in the B-Complex area is shown in Figure 2.1. The B-Complex area includes the B-, BX- and BY-tank farms, each containing 12 large single-shell waste storage tanks, labeled as B-, BX- and BY-101 to 112. The B-tank farm also contains 4 smaller waste storage tanks, labeled as B-201 to B-204. ERT imaging feasibility and performance simulations described in this report were conducted for fictitious leaks from tanks B-102 and B-108.

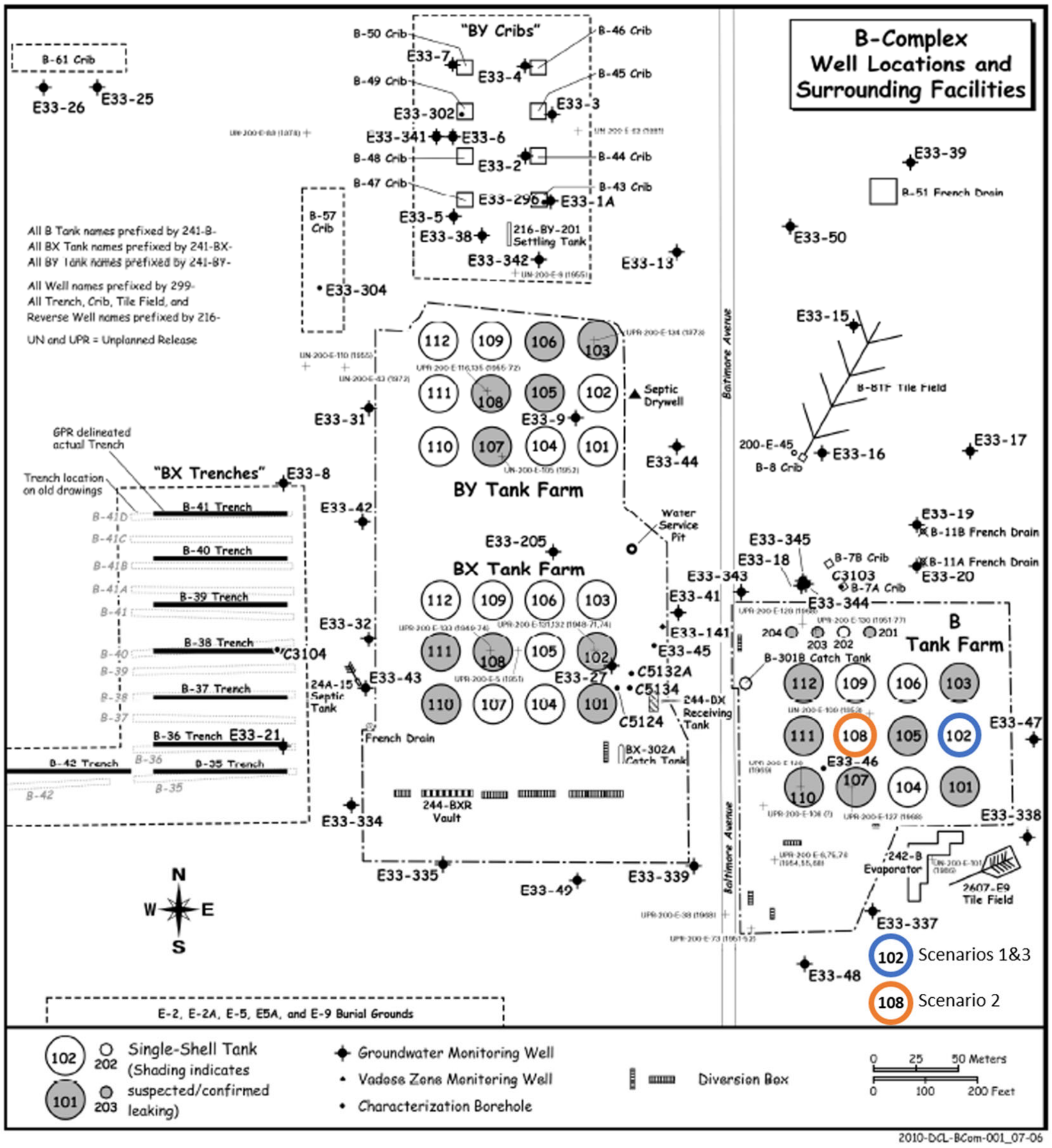

Figure 2.1. Map of the B-Complex area showing key facilities (Serne et al. 2010). Tank B-102 (circled in blue) was used as the leak site for Scenarios 1 and 3. Tank B-108 (circled in orange) was used as the leak site for Scenario 2.

An enlarged map of the B-tank farm region showing key components for the ERT simulation is given in Figure 2.2. The metallic infrastructure in the B-tank farm region includes (1) 12 large buried metal storage tanks (B-101 to B-112) and 4 small buried metal tanks (B-201 to B-204), (2) buried conductive pipes that connect the tanks for water and waste transfer, and (3) metal-cased dry monitoring wells. Figure 2.2 also shows the locations of vertical ERT electrode arrays used in the hypothetical simulations. Imaging performance was assessed using two, four, and eight arrays around each tank, with each array containing 24 equally spaced electrodes from the bottom of the tank to the water table.

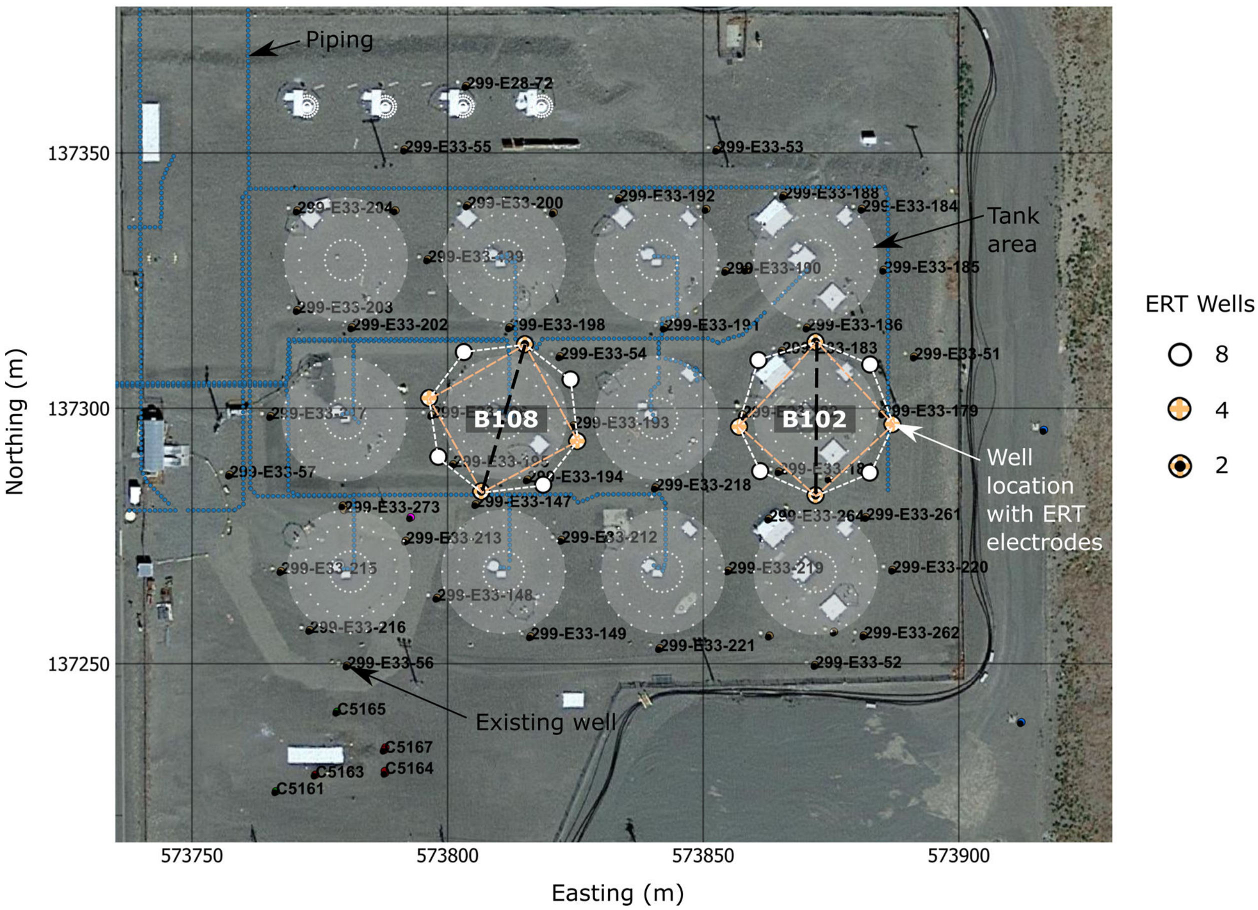

Figure 2.2. Map of the B-tank farm showing borehole locations and metallic infrastructure represented in the simulations. Eight-, four-, and two-well configurations containing borehole ERT arrays are shown surrounding tanks B102 and B108 with dashed white, orange, and black lines connecting each well configuration. There are overlapped boreholes in the eight-, four-, and two-well configurations. Existing wells are labeled and shown as black circles. Transfer piping connecting the tanks are shown as blue circles.

3.0 Electrical Resistivity Tomography

Electrical resistivity (the inverse of electrical conductivity) quantifies how strongly a material opposes the flow of an electrical current. This is controlled by porosity, moisture content, temperature, pore water fluid conductivity, and soil texture. ERT is an active source geophysical method that uses an array of electrodes to image subsurface bulk EC. For a given measurement, two electrodes within the array are used to inject a direct current into the subsurface and two other receiving electrodes are used to measure the voltage. The basic unit of ERT data is transfer resistance (ohm), which is the measured voltage drop (ΔV) across the receiving electrodes divided by the injected current (I) (Figure 3.1).

ERT measurements collected from borehole electrodes were assumed for the simulations in this report (Figure 3.1). Borehole electrodes are installed along the outer diameter of the well-casing, which must be non-metallic such that the current can penetrate into the surrounding formation; a current injected along metallic well casing will preferentially flow along the casing. Borehole electrodes are left in place to monitor changes from an initial state. This is known as time-lapse ERT and it offers an advantage over static imaging because the competing effects of lithology, porosity, and other static geologic background can be eliminated by focusing on changes in bulk EC over time rather than on absolute bulk EC (Singha et al. 2015).

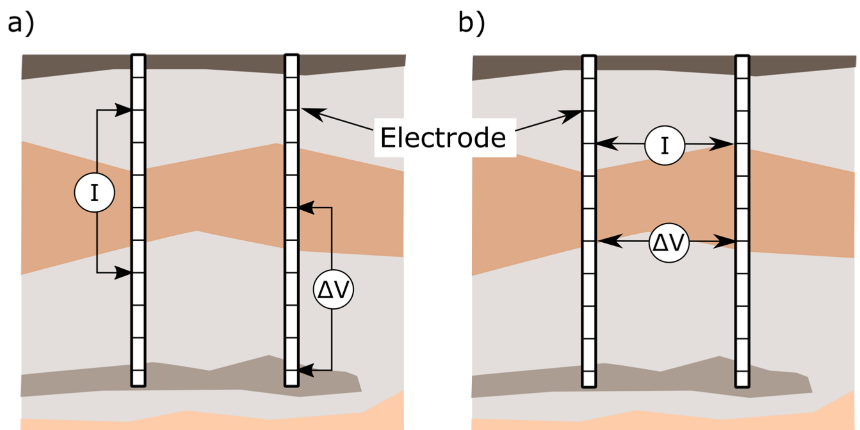

Figure 3.1. Borehole schematic showing example cross well ERT data collection with the current injection in a single borehole a) versus a cross-well injection b).

The spacing between the current-injection and receiving electrodes determines the spatial resolution and volume of interrogation of each measurement. Electrodes with spacings that are farther apart sample a larger volume with lower spatial resolution. In comparison, closer spaced electrodes sample a smaller volume with higher spatial resolution. This general principle was used in the ERT survey design for these simulations to optimally resolve targeted subsurface locations.

Imaging resolution is governed by many factors, including electrode spacing, proximity to electrodes, background electrical noise, and measurement sequence. Bulk EC distribution impacts imaging resolution as this controls how and where electrical current flows in the subsurface. For example, a highly conductive layer would likely be better delineated than a lower conductivity layer due to more current flow in the high-conductivity layer. For the cross borehole measurements simulated in this study, resolution would be highest closer to the boreholes and decrease as the distance from the electrodes increases.

Limited resolution effects are important to consider when interpreting ERT images. In particular, the footprints of bulk EC plumes are likely to appear larger in the ERT images than they are in reality, and the outer extents of plumes will typically bound the true extents, assuming the plume is within the zone of investigation. Small-scale features may also not be resolved and larger resolvable features will be manifest as smoothed or blurred versions of the actual subsurface bulk EC.

Buried metallic infrastructure (refer to Figure 2.2), such as well casings, pipes, and tanks, redistributes subsurface current flow during ERT measurements and can significantly impact resulting images. If metallic subsurface features are not modeled correctly, anomalously high conductivity features will appear in the vicinity of the infrastructure to match the ERT measurements. Johnson and Wellman (2015) demonstrated a method of removing the effects of buried infrastructure by explicitly modeling the infrastructure in the forward modeling phase of the ERT imaging algorithm. This method was used in these simulations to model metallic infrastructure.

4.0 Simulation Details

To evaluate ERT for monitoring tank leaks through the vadose zone, flow and transport simulations provide input into a workflow that translates porosity and concentration to resistivity signals via petrophysical relationships (see Section 4.2). To this end, simulations of contaminant transport from the tanks through the vadose zone were performed using the Richards flow mode and Global Implicit Reactive Transport mode of PFLOTRAN (https://www.pflotran.org, Hammond et al. 2014; Lichtner et al. 2015). ERT imaging simulations were conducted using E4D (https://e4d-userguide.pnnl.gov, Johnson et al. 2010), an open source 3D modeling and inversion code designed to run on distributed memory parallel computing systems.

The PFLOTRAN simulator uses a 3D structured grid with orthogonal, hexahedral grid blocks, while E4D discretizes the model space with a 3D unstructured tetrahedral mesh. Therefore, PFLOTRAN output was interpolated to the E4D mesh. The mesh interpolation scheme of Johnson et al. (2017) was adapted so that each E4D element was divided into sub-elements, and tri-linear interpolation was used to map the PFLOTRAN simulation results to the E4D computational mesh. Next, a petrophysical transformation was used to convert concentration and saturation to the “true” bulk EC vs. time, which were the models by which ERT feasibility was evaluated. ERT data was simulated from these “true” bulk EC models and a time-lapse ERT inversion produced “imaged” bulk EC vs. time. The ERT “imaged” bulk EC vs. time were compared to the “true” bulk EC vs. time to evaluate if the ERT images provided enough information to justify the cost of field implementation (Figure 4.1). Details are provided in the following sections.

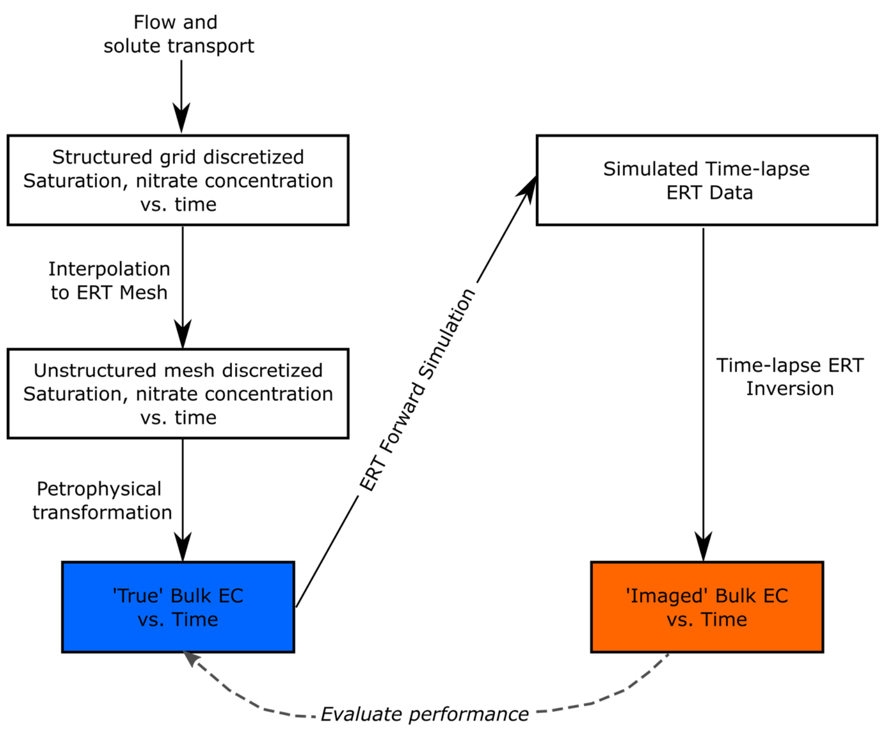

Figure 4.1. ERT performance assessment flow chart.

Three hypothetical scenarios that differ by the quantity of subsurface metallic infrastructure and contaminant leak rate/amount were simulated in the feasibility study. The first two scenarios assumed the same contaminant leak rate and amount (i.e., leak between 1/1/1951 and 12/31/1951 at the rate of 347 m^3 per year) but with different leaky tanks for each scenario. Scenario 1 assumed leaks under tank B-102, which is located on the edge of the B-tank farm and surrounded by a few metallic infrastructure including cased pipes/wells/tanks. Scenario 2 assumed leaks under tank B-108, which is located near the center of the B-tank farm and surrounded by larger amount metallic infrastructure than B-102. Scenario 3 assumed the same metallic infrastructure as B-102 with a more recent contaminant leak between 1/1/2018 and 12/31/2023 at the rate of 1.89 m^3 per year. In each scenario, ERT feasibility was evaluated for electrodes in two-, four- and eight-borehole configurations surrounding the leak tank.

4.1 Flow and Transport

The PFLOTRAN-based flow and transport model was based on the geologic framework model for the site (Springer 2018) and hydraulic properties reported in Serne et al. (2010). The same model configuration (e.g., boundary conditions, hydrostratigraphic units, hydraulic parameters) was used for each scenario, and only differed in the simulated leak location and rate. The model domain spans 800 m, 800 m, and 95 m in the easting, northing, and vertical directions, respectively, covering the 116 to 221 m elevation range. The domain was discretized into 144, 144, and 181 grid blocks in the easting, northing, and vertical directions, respectively, for a total of ~1.7M grid blocks. Grid blocks lying above the top of the ground surface were specified as inactive. Non-uniform grid spacing was used in all directions, with grid block sizes ranging from 4 to 10 m in the easting and northing directions, and 0.1 to 2 m in the vertical direction.

Figure 4.2 is a cutaway view through the model domain showing the hydrostratigraphic units. From top to bottom, the hydrostratigraphic units include a thick sequence of highly permeable unconsolidated sands and gravels of the Pleistocene-age Hanford formation (units H1, H2, H3), deposited during a series of mega-floods. The H2 unit has been subdivided into coarse (C) and lower-permeability fine (F) grained subunits (Serne et al. 2010). The Hanford formation is underlain by fluvial and lacustrine deposits of the Pliocene-age Cold Creek unit (CCU), which contains silt- (CCUz), sand- (CCUz_sand), and gravel-dominated (CCUg) subunits (Oostrom et al. 2013; Springer 2018). A low-permeability subunit of CCU was included in the model to represent the perched water aquifer (Perchisilt) identified in the field. The CCU is underlain by various subunits of fluvial and lacustrine deposits of the semi-consolidated Pliocene-age Ringold Formation, including the Taylor Flat member, and unit E, Lower Mud unit, and unit A. Although present over a large area of the Hanford Site, the Taylor Flat member, unit E, and Lower Mud unit are absent in the immediate vicinity of the domain investigated for this study, so these units are not shown in Figure 4.2. The Ringold Formation is underlain by basalt of the Columbia River Basalt Group.

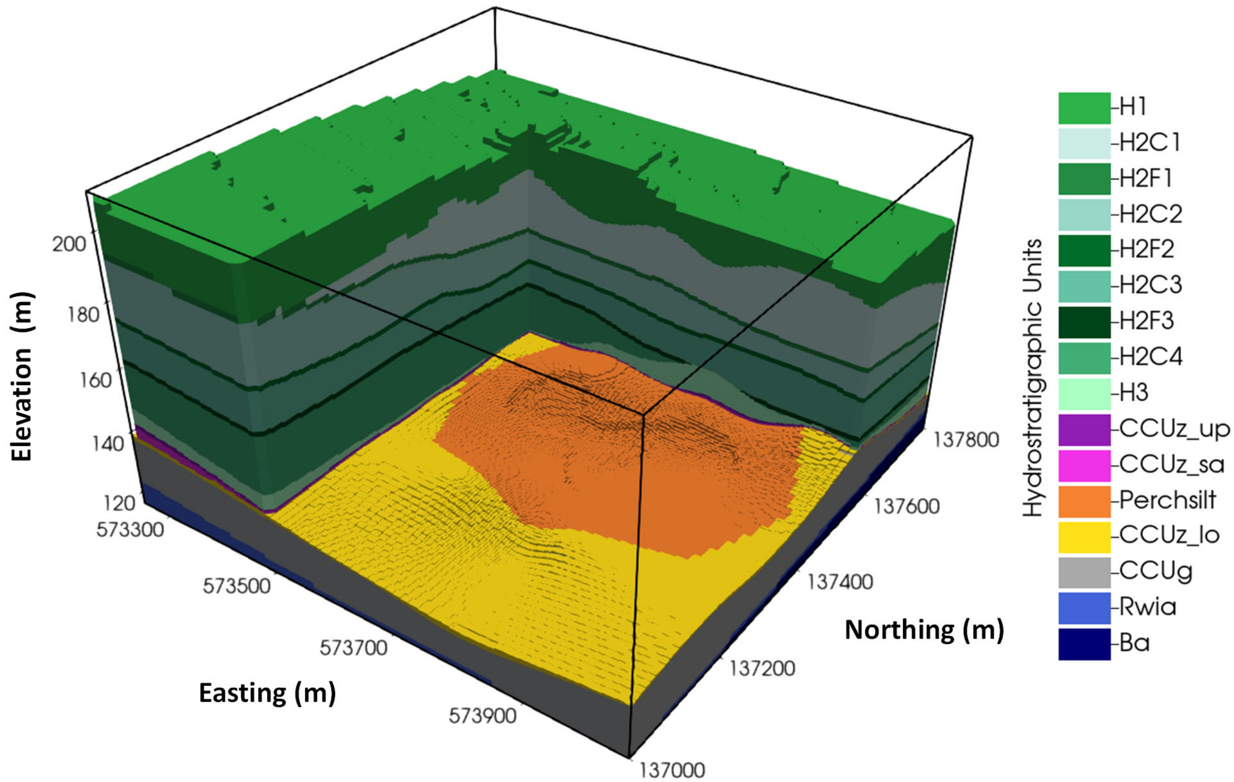

Figure 4.2. Hydrostratigraphic units underlying the B-Complex area used in flow and transport modeling.

Physical and hydraulic properties that were assigned to the hydrostratigraphic unit for flow and transport modeling are provided in Table 4.1. These parameters were based on prior modeling efforts and site characterization data (Oostrom et al. 2013, 2017). The parameters k_x, k_y, and k_z are the permeability in the easting, northing, and vertical directions, respectively. The parameters θ_s, S_r, α, and n are the saturated water content, residual saturation, and two water retention parameters for the van Genuchten (1980) model, respectively. The α parameter is the inverse of the air-entry pressure, and the n parameter affects the slope of the water retention function for the porous media. The parameter ρ_s is the grain density.

Table 4.1. Hydraulic and physical properties of hydrostratigraphic units used for modeling subsurface flow and transport at the B-Complex.

Formation	Unit	k_x, k_y (m^2)	k_z (m^2)	θ_s	S_r	α (m^{-1})	n	ρ_s (kg m^{-3})
Hanford	H1	2.72E-12	6.79E-13	0.280	0.140	1.400	2.120	2590
	H2C1	9.27E-12	2.32E-12	0.386	0.077	6.100	2.030	2620
	H2F1	3.82E-15	3.82E-15	0.406	0.084	0.270	2.170	2620
	H2C2	9.27E-12	2.32E-12	0.386	0.077	6.100	2.030	2620
	H2F2	3.82E-15	3.82E-15	0.406	0.084	0.270	2.170	2620
	H2C3	9.27E-12	2.32E-12	0.386	0.077	6.100	2.030	2620
	H2F3	3.82E-15	3.82E-15	0.406	0.084	0.270	2.170	2620
	H2C4	9.27E-12	2.32E-12	0.386	0.077	6.100	2.030	2620
	H3	2.72E-12	6.79E-13	0.280	0.140	1.400	2.120	2590
Cold Creek	CCUz_up	5.69E-14	5.69E-14	0.404	0.097	0.500	2.250	2820
	CCUz_sa	1.21E-13	1.21E-13	0.252	0.134	1.700	1.730	2820
	Perchsilt	1.02E-16	1.02E-16	0.376	0.066	0.46	1.767	2710
	CCUz_lo	5.69E-14	5.69E-14	0.404	0.097	0.500	2.250	2820
	CCUg	3.37E-13	3.37E-13	0.258	0.134	1.700	1.730	2630
Ringold	Rwia	1.18E-12	1.18E-13	0.200	0.056	1.970	1.419	2710
Basalt	Ba	1.65E-17	1.65E-17	0.100	0.073	2.100	1.374	2710

Hydrostatic boundary conditions were applied to the lateral sides of the model domain for the flow equation by assuming a constant groundwater table at 121 m. A constant recharge rate, 2.8 mm/yr, was applied to the top of the model domain. This recharge value is estimated by Fayer and Keller (2007) for undisturbed areas with sandy loam soil and shrub vegetation area in this site. The lower boundary of the model was treated as no-flow as it is underlain by the basalt with low permeability. The transport conditions for the lateral inland boundaries were set as zero dispersive gradients for outflow and zero concentration tracer for inflow. The recharge of the top boundary contains no solutes (e.g., NO_3-). A 1,000,000-year flow-only simulation was used to achieve a steady-state before modeling the tank-leaking period. Then, three flow and transport cases were designed to represent tank leaking scenarios, as shown in Table 4.2. The tank leaking was modeled as a point source under the tank. The model top boundary and side boundaries remained constant throughout the steady-state and tank leak simulations.

Table 4.2. Tank leaking scenarios.

Scenario Designation	Location	Start of Leak (dd/mm/yy)	End of Leak (dd/mm/yy)	Leaking Volume (m^3/yr)	NO_3- Concentration (kg/m^3)
1	B-102	1/1/1951	12/31/1951	347	10.95
2	B-108	1/1/1951	12/31/1951	347	10.95
3	B-102	1/1/2021	12/31/2023	1.89	10.95

4.2 Petrophysical Transformation

PFLOTRAN outputs parameters of liquid saturation S, porosity ϕ (which equal the saturated water content θ_s in Section 4.1) and contaminant concentrations that are transformed into bulk EC, σ_b, for the ERT simulations. For a partially saturated electrically resistive sediment, Archie's law (Archie 1942) describes the relationship between σ and pore space properties as

$$\sigma_b = \sigma_w \phi^m S^n \tag{4.1}$$

Surface conduction is assumed to be negligible in Eq. (4.1), which is valid to a first-order given that the target zones are within the Hanford formation, which contains mostly coarser sediments. The cementation exponent m is a function of the rate of change in pore complexity with porosity (Yue 2019), dependent on particle shape and orientation (Niu and Zhang 2018) and typically varies between 1.2 and 4.4 (Lesmes and Friedman 2005). The cementation exponent was set equal to 1.3 for these simulations based on previous work (Robinson et al. 2020). The saturation exponent n is associated with the additional tortuosity due to the replacement of pore fluid with air (an insulator). Commonly, n = 2 is used and was also assumed in this assessment (e.g., Brunet et al. 2010; Day-Lewis et al. 2005).

Three contaminant concentrations were output from PFLOTRAN: total nitrate (NO_3), technetium-99, and total uranium. Since out of these three, nitrate has a high ionic fluid conductivity, this output fluid concentration was converted to σ_w in Eq. (4.1) as

$$\sigma_w = \sigma_{GW} \cdot \left(1 - \frac{c_{NO3}}{\max(c_{NO3})}\right) + \sigma_{NO3} \cdot \left(\frac{c_{NO3}}{\max(c_{NO3})}\right) \tag{4.2}$$

where σ_{GW} is the groundwater conductivity, σ_{NO3} is the nitrate conductivity, and c_{NO3} is the total nitrate concentration. According to this equation, σ_w equals to σ_{NO3} where the nitrate reaches the maximum concentration and equals to σ_{GW} in places where there is no nitrate. For the total nitrate concentration between 0 and the maximum value, the converted fluid conductivity falls to an intermediate value between σ_{GW} and σ_{NO3}. It was assumed σ_{GW} was equal to 0.008 S/m and σ_{NO3} was equal to 10 S/m in Eq. (4.2) (Rucker et al. 2013). Note that not all contaminant concentrations were considered in σ_w, as the σ can still be impacted through changes in saturation.

When substituting Eq (4.2) into (4.1) and using $m = 1.3$ and $n = 2$, the final equation to convert c_{NO3}, ϕ, and S simulated by PFLOTRAN to σ_b is written as

$$\sigma_b = \sigma_w \phi^{1.3} S^{2.0} + 0.001 \tag{4.3}$$

where σ_w is defined in Eq. (4.2) and units of S/m are assumed for bulk and fluid conductivities. The second term in Eq. (4.3) was used to adjust the bulk EC in the background to an average Hanford formation conductivity of 0.001 S/m (Johnson and Wellman 2013).

4.3 Electrical Resistivity Tomography

The model domain is shown in Figure 4.3, which includes the following metallic infrastructure: (1) 12 large buried metal storage tanks (B-101 to B-112; 24 m x 24 m x 10 m) and 4 small buried metal tanks (B-201 to B-204; 4.2 m x 4.2 x 1.74 m); (2) buried transfer pipes; and (3) metal-cased wells. In the E4D finite element mesh, the metallic infrastructure is explicitly included and incorporated into the forward modeling (Johnson and Wellman 2015). The tanks are modeled as hollow cylinders in true dimension with metal shells. The pipes and wells are included in the mesh as point sources with 0.25-m spacing between each node/point along the line. This leads to a refined mesh around the pipes and wells. A total of 68 metal-cased wells were included in the B-tank farm conceptual model. The depths of the wells vary from 12.77 to 82.9 m. Details of the cased wells can be found in Table A.1 in Appendix A. Locations and bottom elevations of the wells are obtained from Hanford Environmental Information System (HEIS) database. Tops of the wells are adjusted to elevation 200 m in compliance with the flat topography in the conceptual model.

The main computational mesh covers an area of 190 m x 185 m and extends from the surface down to a depth of 132 m. The boundaries of the entire mesh extend far beyond the main domain (~5000 m, not shown) to meet the boundary condition requirements in the ERT simulation. The spatial variability of the topography in the B-tank farm region is relatively small, so a flat topography at an elevation of 200 m was used. The main computational mesh includes two zones: (1) a vadose zone of depth 82 m above the water table, and (2) a saturated zone below the water table. The two zones are separated by a flat water table boundary.

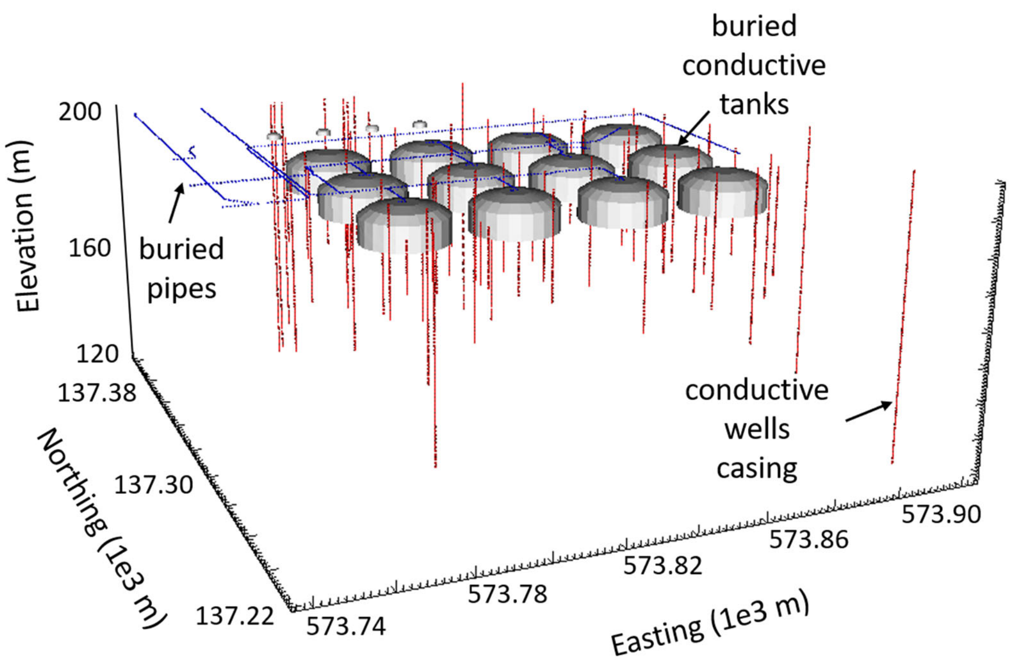

Figure 4.3. Model domain of the B-tank farm showing infrastructure included in the ERT finite element mesh. Buired pipes were shown in blue. Cased wells were shown in red. Buried tanks were shown in gray.

For the ERT simulations, two different unstructured tetrahedral meshes were constructed, one for B-102 simulations and one for B-108 simulations (Figure 4.4). This allowed for refinement of mesh elements beneath each tank, allowing for more accurate forward modeling beneath the tank of interest while reducing computational times that would result from finer elements beneath additional tanks in the farm. The B-102 mesh contained 1.5 million elements and the B-108 mesh contained 1.43 million elements. The differences in the number of elements was mainly a function of the number and depth of wells surrounding each of these tanks.

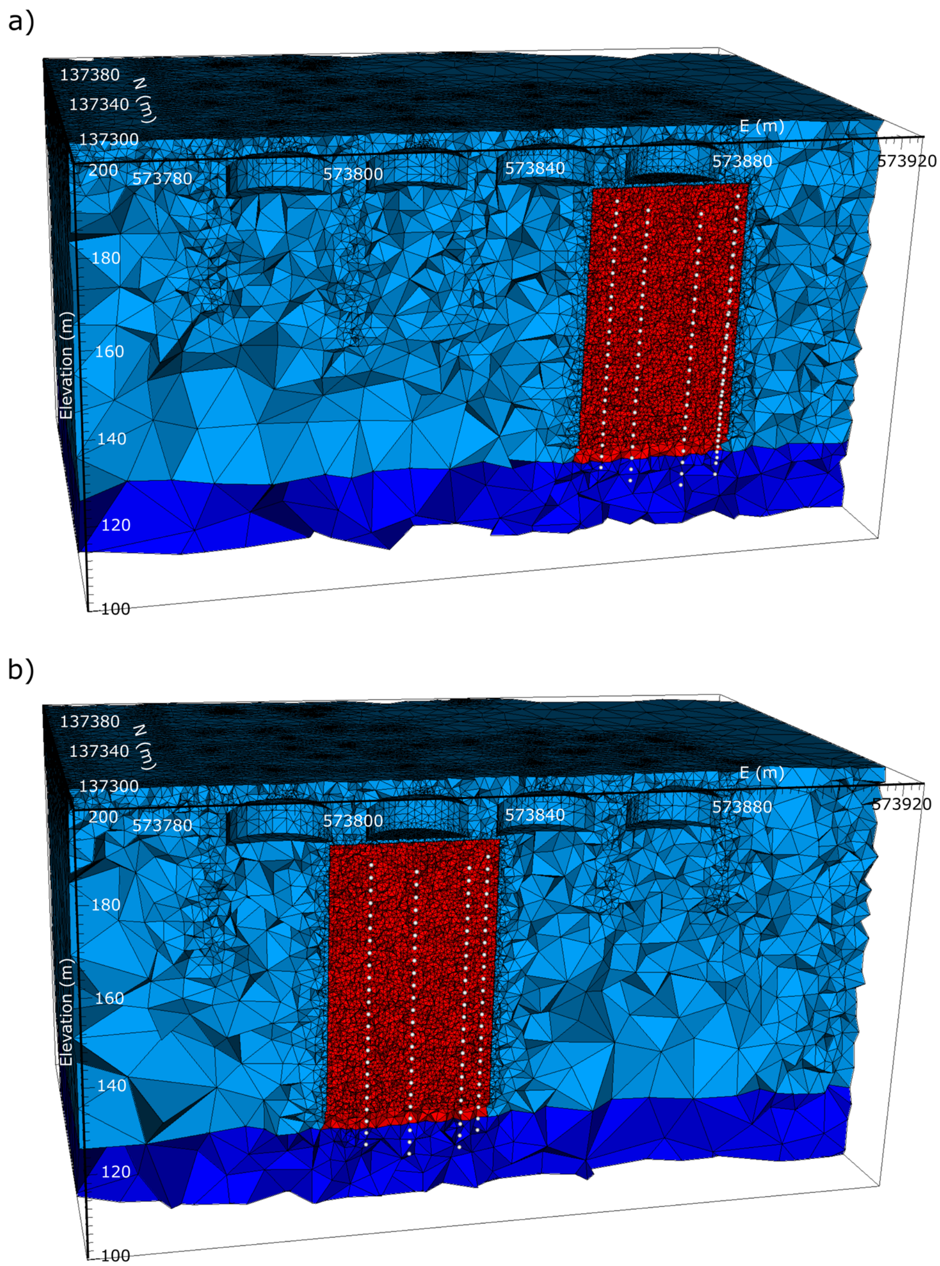

Figure 4.4. Finite element meshes used in the ERT E4D modeling for a) tank B-102 and b) tank B-108. Colors represent different zones used in the mesh where light blue is the vadose zone, dark blue is the saturated zone below the water table, and red is the finely discretized region below the tank.

Electrodes were vertically positioned along hypothetical boreholes surrounding the B-102 and B-108 tanks to avoid existing infrastructure (refer to Figure 2.2). ERT feasibility was evaluated for electrodes in two, four, and eight boreholes surrounding each tank. Table 4.3 summarizes the ERT scenarios. Within each ERT borehole, there were 24 electrodes vertically spaced 2.85 m apart. The top electrode elevation was 184 m, or below the tank bottom. The bottom electrode elevation was 118.45 m, which was slightly above the water table elevation of 118 m.

Table 4.3. ERT simulations overview

Scenario Designation	Location	Description	Summary	ERT simulations
1	B-102	Tank leak from 1/1/1951 to 12/31/1951 at rate 347 m^3/yr, evaluate ERT from 2022-2500 yr	Historical leak from a tank on the edge of the tank farm; contaminant target surrounded by a few metallic infrastructure	Two, four, and eight borehole
2	B-108	Tank leak from 1/1/1951 to 12/31/1951 at rate 347 m^3/yr, evaluate ERT from 2022-2500 yr Same leak parameters as B-102 location with different surrounding metallic infrastructure	Historical leak from a tank near the center of the tank farm; contaminant target surrounded by larger amount of metallic infrastructure than Sceanrio 1	Two, four, and eight borehole
3	B-102	Tank leak from 1/1/2021 to 12/31/2023 at rate 1.89 m^3/yr, evaluate ERT from 2022-2500 yr Same as B-102 location, with different tank leak parameters	New leak from a tank on the edge of the tank farm; contaminant target surrounded by the same metallic infrasctructure as Scenario 1	Two, four, and eight borehole

Forward computations to generate ERT data used a measurement sequence consisting of in-line (1D), cross borehole (2D), and cross multiple-borehole (3D) measurements. Table 4.4 provides a summary of the ERT configuration for the different borehole configurations. Two percent randomly distributed noise was added to the generated data, which is typical of noise levels on the Hanford Site (Robinson et al. 2020).

A background inversion was performed for a synthetic ERT dataset for the year 2021, which represents the earliest time actual ERT measurements could be collected in the field. The background inversion used a spatial nearest-neighbor smoothness constraint. The time-lapse inversions used the background inversion as a reference model, and ERT datasets were inverted for changes from previous models using nearest-neighbor smoothing in space and time. This allows for a smooth transition in bulk EC between surrounding elements and between time steps.

Table 4.4. Borehole configurations for ERT feasibility.

Well Configuration	# electrodes	# ERT Measurements
Two-borehole	48	1090
Four-borehole	96	3388
Eight-borehole	192	11593

5.0 Simulation Results

5.1 Flow and Transport

Scenarios 1 and 2 are identical except for the physical location of the leak. Because of the high concentrations of nitrate in tank waste and its high conductivity, contaminant transport was simulated with nitrate as a surrogate. The resulting nitrate concentrations for these simulations are shown in Figure 5.1a for years 2022, 2045, and 2500. The images show downward and lateral migration of nitrate over time with color scales varying depending on the maximum nitrate concentration.

The transformation of nitrate concentration and saturation to the bulk EC model using Archie parameters according to Eq. (4.3) is shown in Figure 5.1. Nitrate concentrations play a key role in this transformation whereby locations of elevated nitrate concentrations correspond to higher bulk ECs. In addition, higher porosity units can also have a higher bulk EC due to an increase in moisture content. The transformation demonstrates how bulk EC is influenced by nitrate concentration, saturation, and porosity. The resulting bulk EC images (Figure 5.1d) are representative of the location of the nitrate plume plus lithologic properties (e.g., porosity).

The Scenario 3 flow and transport simulations and transformation to bulk EC are shown in Figure 5.2 for years 2022, 2025, and 2200. Preliminary results showed limited contaminant migration below elevation 140 for these simulation times, so the figure is truncated below this elevation to better depict contaminant transport. This figure depicts a dominant downward nitrate transport until high-porosity units are reached. After this, there is lateral migration within the high-porosity unit fluids, increasing bulk EC.

The bulk EC models shown in Figure 5.1 and Figure 5.2 were used to generate synthetic ERT measurements for the performance evaluation.

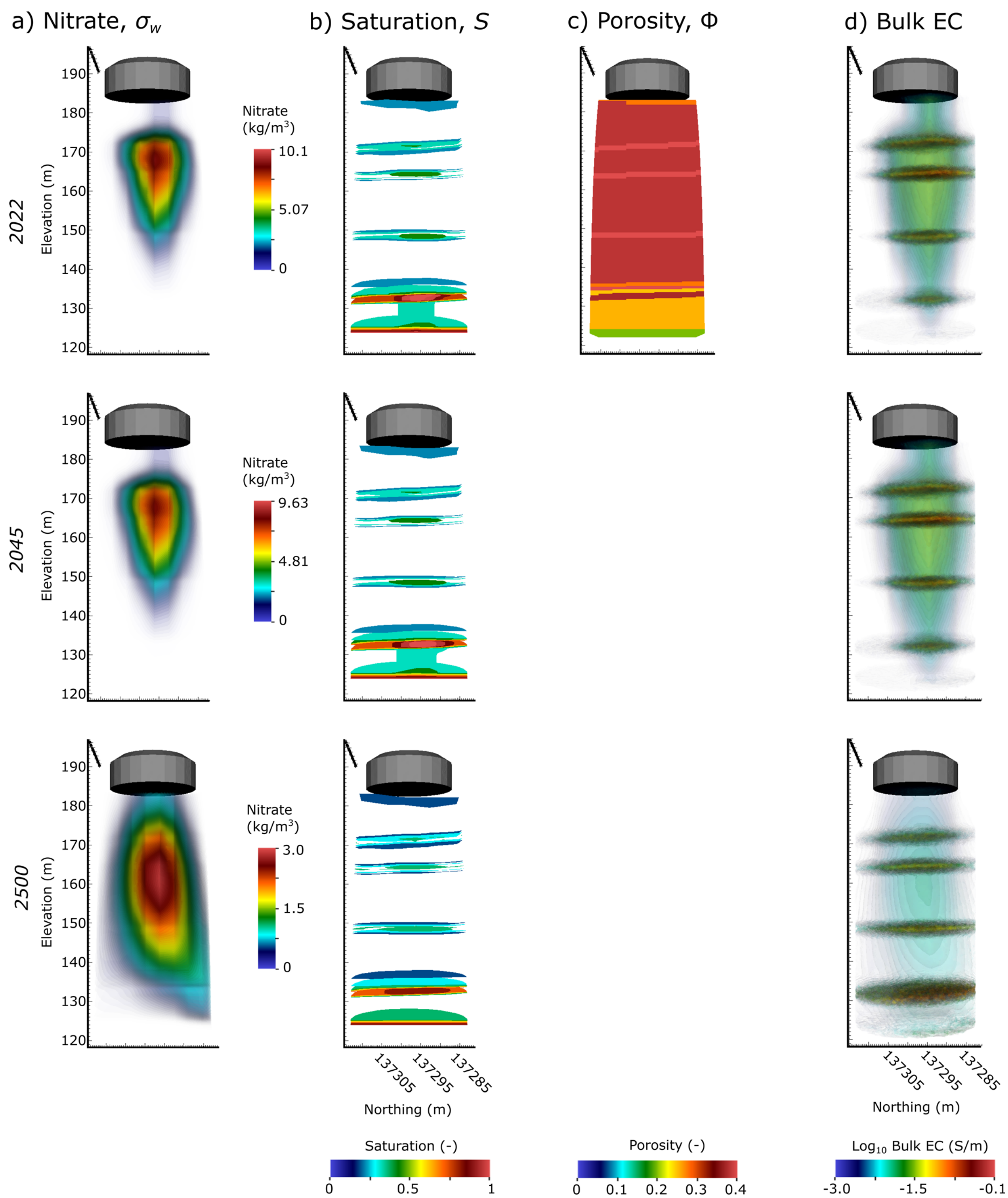

Figure 5.1. Scenarios 1 and 2 flow and transport nitrate concentrations in a), saturation in b), porosity in c), which is constant across all models and the resulting bulk EC models in d) used for the ERT simulations. Nitrate and bulk EC are shown as transparent 3D isosurfaces.

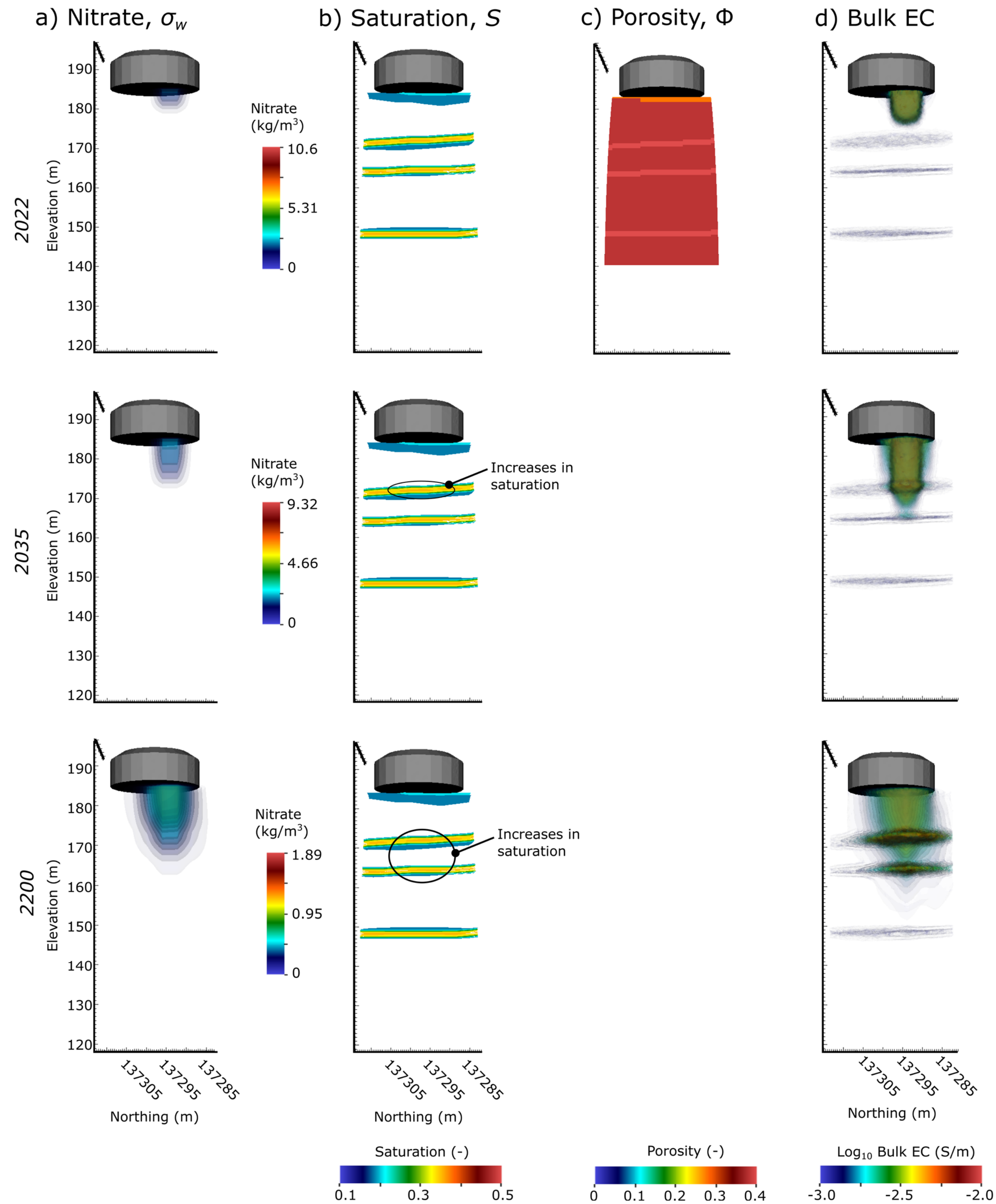

Figure 5.2. Scenario 3 flow and transport nitrate concentrations in a), saturation in b), porosity in c), which is constant across all models and the resulting bulk EC models in d) used for the ERT simulations. Nitrate and bulk EC are shown as 3D isosurfaces. The minimum elevation shown is 140 m.

5.2 ERT Monitoring

For all scenarios in Table 4.3, a baseline ERT image was generated from year 2022 and all subsequent time-lapse datasets were evaluated for changes from this baseline. ERT monitoring images are shown as 3D isosurfaces of bulk EC alongside eight-, four-, and two-array ERT images in Figure 5.3 through Figure 5.5. Color scales were chosen to highlight variability. The display years were chosen to highlight maximum changes over time. Figure 5.3 and Figure 5.4 (Scenarios 1 and 2) highlight differences in ERT images due to the presence of surrounding metallic infrastructure (see Figure 2.2). Figure 5.3 and Figure 5.5 (Scenarios 1 and 3) highlight differences in the ERT images due to changing leak parameters (see Table 4.2).

Generally, the eight-borehole ERT images display the most detail and can image migration within the high porosity stratigraphic units better than the four- and two-borehole ERT. However, the four-borehole ERT images do well with the overall delineation, and better than the two-borehole ERT. The two-borehole ERT shows changes for Scenarios 1 and 2, but exhibits relatively poor early-time resolution when the leakage volume is lower in Scenario 3.

The ERT images have limited ability to show changes directly beneath the leaky tanks in the simulations to varying extent. This lower resolution is due to the presence of the tank itself, whereby current preferentially flows toward and within the metallic tank and not within the surrounding sediments. This is particularly evident in the two-borehole ERT Scenario 3 results.

The metallic casings and surrounding infrastructure have limited impact within the ERT images, and it is difficult to distinguish the difference between Figure 5.3 and Figure 5.4. Changes in the volume and leakage rate (e.g., Scenario 1 vs. 3) have a more profound influence on the ERT images. In Scenario 3, the eight-borehole ERT images produce more detail than the four- or two-borehole configurations.

The ERT images highlight both the strength and limitations of this method and associated E4D modeling. For example, a strength is that, in all cases, ERT can detect a change in the bulk EC due to the tank leak constituents at depth using an array of borehole electrodes. Visualization of these changes would provide 3D subsurface information for decision-making that is not available through borehole sampling or surface imaging. However, a limitation is that ERT images appear vertically and laterally smeared compared to the bulk EC models, and this is due to the survey geometry, measurement errors, physical limitations of the electrical method, and the nearest-neighbor smoothness constraints applied in the E4D inversions. In addition, there is limited ability of ERT to resolve sharp boundaries of thin stratigraphic units without explicitly including these in the modeling. This information was not included in these simulations because it is not known. ERT provided a blurred representation of the bulk EC models; however, the ERT images contain the information necessary to identify the plume footprint.

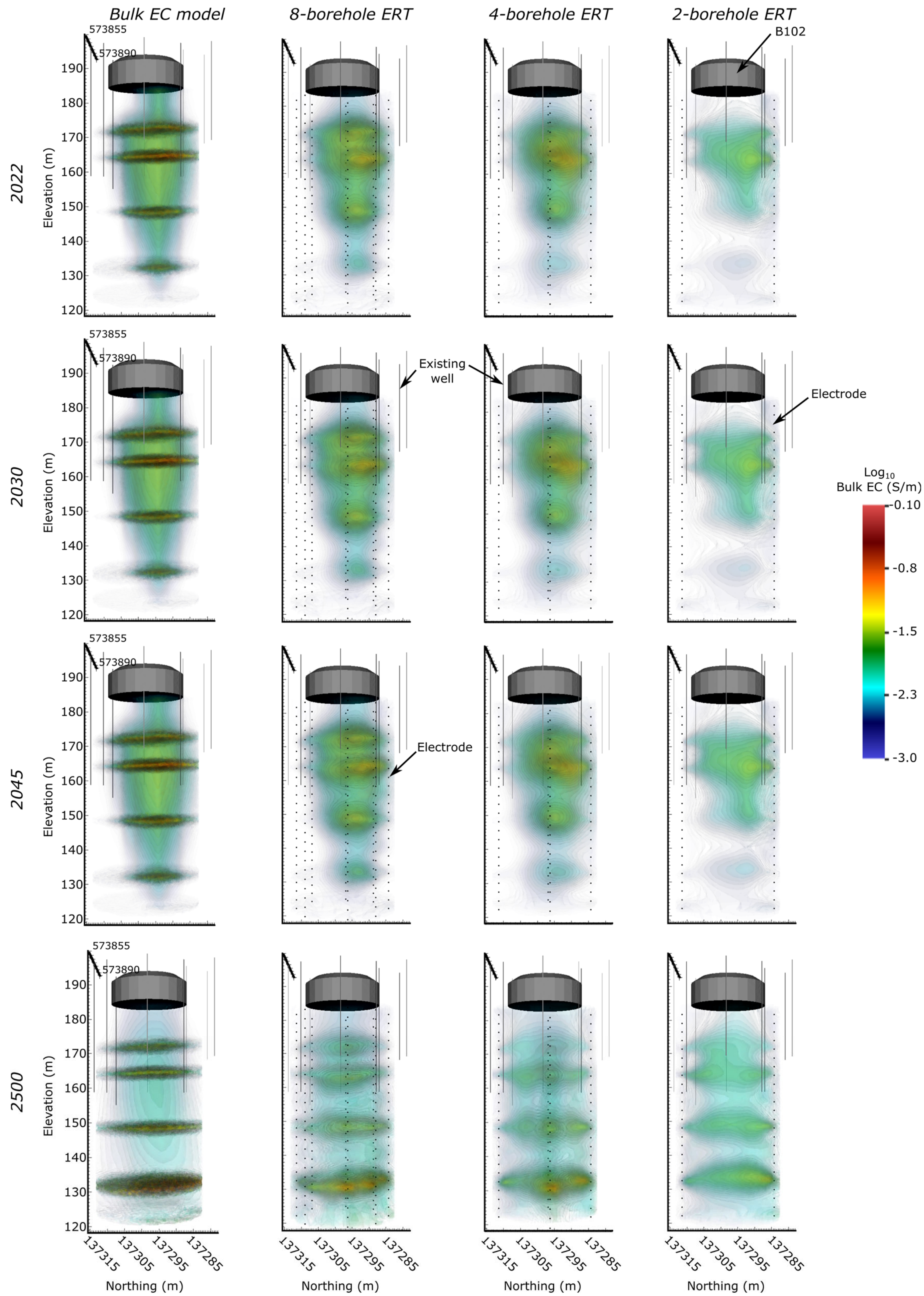

Figure 5.3. Scenario 1 time-lapse ERT monitoring shown as 3D isosurfaces beneath B-102 for electrodes positioned in eight boreholes, four boreholes and, two boreholes for years 2022, 2030, 2045, and 2500.

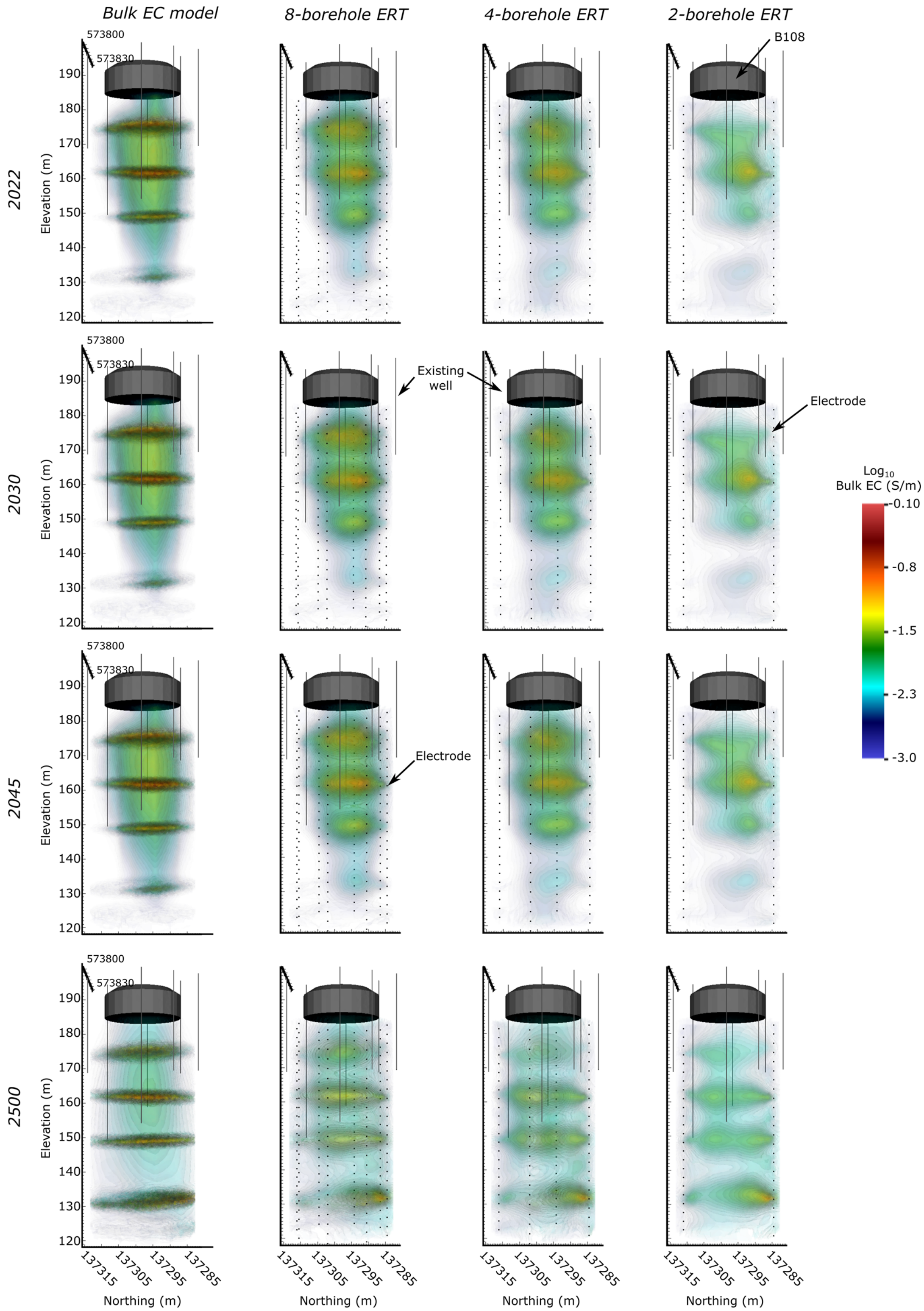

Figure 5.4. Scenario 2 time-lapse ERT monitoring shown as 3D isosurfaces beneath B-108 for electrodes positioned in eight boreholes, four boreholes, and two boreholes for years 2022, 2030, 2045, and 2500.

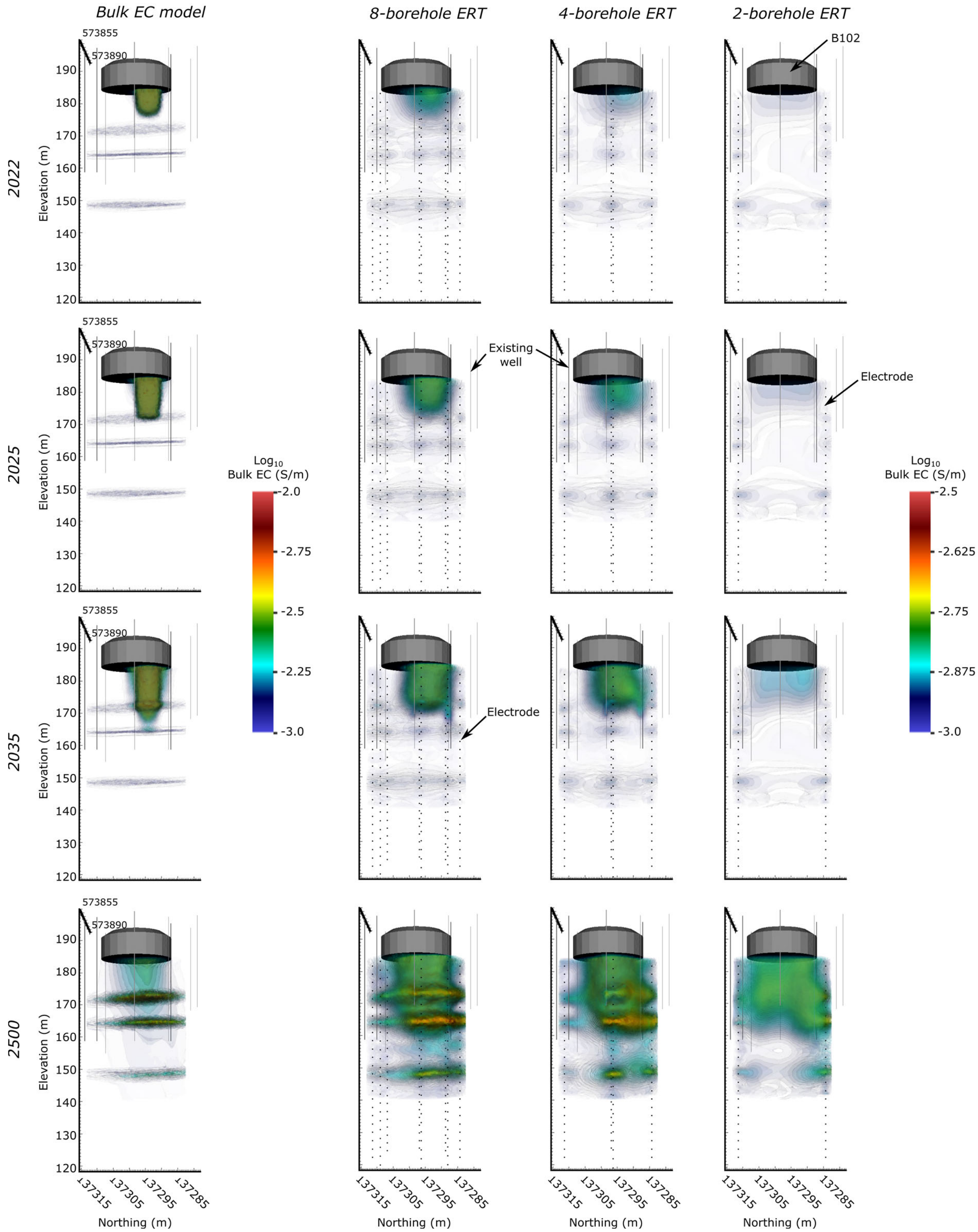

Figure 5.5. Scenario 3 time-lapse ERT early-time leak monitoring shown as 3D isosurfaces beneath B-102 for electrodes positioned in eight boreholes, four boreholes, and two boreholes for years 2022, 2025, 2035, and 2500.

6.0 Installation Options and Hardware Costs

Vertical electrode arrays can be installed using direct push methods or traditional rotary drilling. Direct push methods work by driving a hollow steel tube (typically 2 to 3 inches in diameter) vertically into the subsurface using direct force, rotation, vibration, or hammering, or any combination of these. Once the tube has been installed to the target depth, an ERT cable with integrated electrodes is lowered down the center of the tube. An electrically resistive grout is used to seal the electrodes in place as the drive tube is extracted, leaving only the electrodes, cable, and grout seal as shown in Figure 6.1. Direct push installations produce no soil cuttings and generally require less heavy machinery within the tank farm boundaries. They have been used to successfully install electrode cables at the Hanford Site. However, installations can experience refusal in the presence of cobbles and coarse gravels.

Borehole installations use traditional rotary drilling methods, whereby a drill casing is advanced behind a drill bit as cuttings are transported to the surface. When drilling is complete, the drill bit and stem are extracted, and the drill casing holds the borehole open while the electrode array is installed. During installation, stainless steel electrodes are attached to an inner, non-metallic liner as it is lowered into the drill casing. Each electrode is attached to an ERT cable that extends to the surface through the annulus. Once the liner and electrodes have been emplaced, the drill casing is extracted as the annulus is sealed with an electrically resistive grout, producing a final non-metallic borehole and annular electrode array as shown in Figure 6.1. In contrast to direct push installations, borehole installations produce a sealed borehole that can be used for other contaminant sensing modalities such as gamma ray logging. Additionally, borehole installations are generally immune to refusal during installation. However, they do produce drill cuttings, which may be contaminated (thereby requiring health and safety mitigation and disposal) and require heavier equipment than direct push installation.

Both installation types leave a cable and cable head at the surface that extends to ERT survey instrumentation. Cables can be stored (for example) within flush mount boxes at each borehole or run through conduits to the outside of the tank farm fence line. In either case, cables can be extended so that ERT surveys can be conducted from beyond the tank farm boundary/fence line, thereby reducing manual labor and risks of exposure. ERT monitoring can be conducted autonomously or by periodic onsite visits as desired. Autonomous monitoring requires no human presence on site, and continuous data acquisition is possible. For periodic onsite visits involving a field crew, a typical ERT survey (e.g. as shown in this report) is anticipated to require 4-8 person hours total.

Non-maintainable parts of the ERT array (i.e., electrodes and cables) can be made of robust materials designed for long-term buried applications with a design life of at least 50 years. For information only, hardware costs for the ERT system alone are typically $600 to $800 per electrode as of 2021. This translates to $38.4K to $48.0K, $76.9K to $96.0K, and $153.6K to $192.0K for the two-, four-, and eight-borehole arrays presented in this report. These costs are likely a fraction of the costs required for the array installation within the tank farm boundaries. One-time installation costs including drilling are not estimated in this report, but are anticipated to be the largest cost incurred by far for the lifetime of the ERT monitoring system.

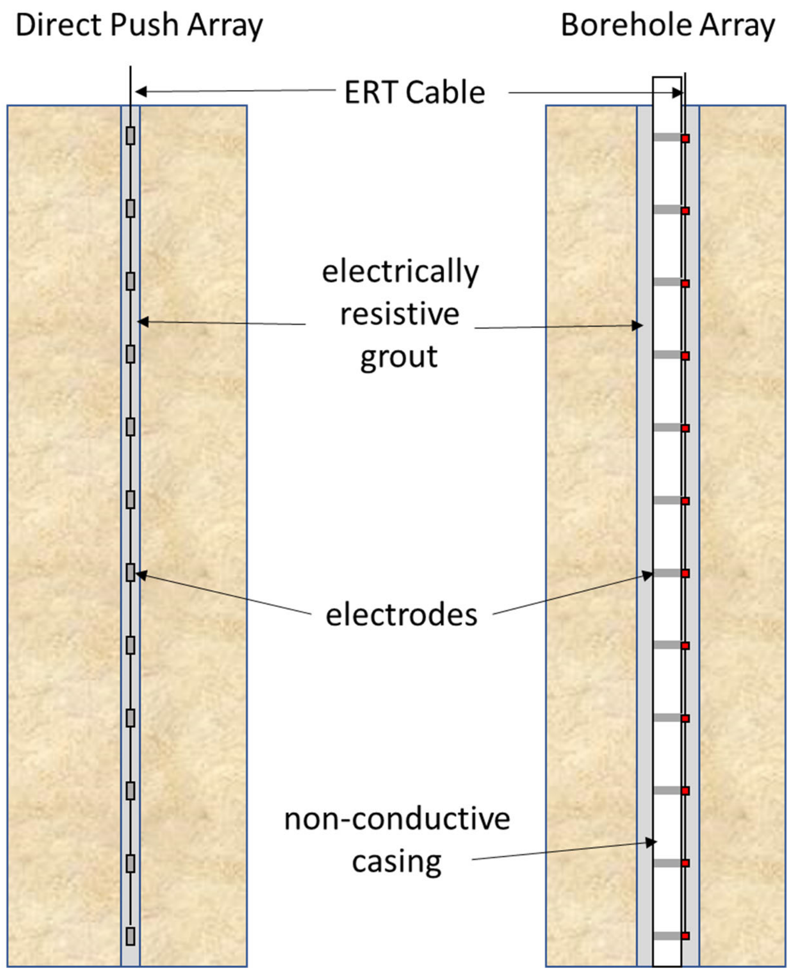

Figure 6.1. Vertical ERT array diagrams for (left) direct push and (right) borehole electrode installations (not to scale).

7.0 Summary and Conclusions

The release of liquid tank wastes increases subsurface fluid conductivity and saturation over time, creating a target to use time-lapse ERT for long-term monitoring. This report demonstrated the use of ERT electrodes in vertical wells to monitor tank waste location and migration through the vadose zone. E4D allows metallic infrastructure to be incorporated within the modeling, which increases the utility of ERT in the vicinity of tanks, piping, and metallic well casings. The three simulated configurations of wells used (two, four, and eight wells) were able to successfully monitor tank leak migration; however, bulk EC resolution increased with the number of ERT imaging wells. Therefore, eight ERT well arrays were able to provide the best spatiotemporal information. For all configurations, the volume from approximately 2 to 4 m beneath the tank was less resolved due to the presence of the electrically conductive tank.

The primary cost for long-term ERT monitoring is likely the upfront cost associated with the direct-push or drilling inside of the tank farm boundaries, which is anticipated to far exceed costs for ERT hardware, data collection, data processing, and reporting. In terms of system longevity, non-maintainable components of the system include the vertical arrays, which are composed of buried insulated cables and metal electrodes. Consequently, system longevity is directly related to electrode and cable corrosion rates. Appropriately designed cables and electrodes are anticipated to last at least 5 decades based on industry standards for buried cable design.

Although site-specific conditions for a given implementation are likely to differ from the assumptions used in this document, the performance of ERT for monitoring waste releases through the vadose zone has been well demonstrated. Identifying source arrivals to groundwater can help manage groundwater treatments, such as pump-and-treat and monitored natural attenuation. Once the ERT boreholes and arrays are in place, imaging data can be collected at specified intervals from outside of the tank boundaries (assuming ERT cable heads are located outside of the fence line). Once the initial data processing routine is set up, data analysis is autonomous. This eliminates the need for human presence on site and provides the capability to both monitor the distribution and migration of contaminants from pre-existing leaks as well as monitoring for new leaks.

8.0 Quality Assurance

This work was performed in accordance with the Pacific Northwest National Laboratory (PNNL) Nuclear Quality Assurance Program (NQAP). The NQAP complies with the United States Department of Energy Order 414.1D, *Quality Assurance*. The NQAP uses NQA-1-2012, *Quality Assurance Requirements for Nuclear Facility Application* as its consensus standard and NQA-1-2012 Subpart 4.2.1 as the basis for its graded approach to quality.

This work emphasized acquiring new theoretical or experimental knowledge. The information associated with this report should not be used as design input or operating parameters without additional qualification.

9.0 References

Archie GE. 1942. "The Electrical Resistivity Log as an Aid in Determining Some Reservoir Characteristics." *Transactions of the AIME* 146(01):54-62. doi:10.2118/942054-G

ASME NQA-1-2012, *Quality Assurance Requirements for Nuclear Facility Application*. American Society of Mechanical Engineers, New York, NY.

Brunet P, R Clément, and C Bouvier. 2010. "Monitoring soil water content and deficit using Electrical Resistivity Tomography (ERT) – A case study in the Cevennes area, France." *Journal of Hydrology* 380(1):146-153. https://doi.org/10.1016/j.jhydrol.2009.10.032

Day-Lewis FD, K Singha, and AM Binley. 2005. "Applying petrophysical models to radar travel time and electrical resistivity tomograms: Resolution-dependent limitations." J*ournal of Geophysical Research: Solid Earth* 110(B8). https://doi.org/10.1029/2004JB003569

DOE Order 414.1D, *Quality Assurance*. U.S. Department of Energy, Washington, D.C.

Ecology. 2021. "Ecology tracking Hanford waste tank leak." News release, April 29, 2021. Washington State Department of Ecology, Olympia, WA. https://ecology.wa.gov/About-us/Who-we-are/News/2021/Ecology-tracking-Hanford-waste-tank-leak

Fayer MJ and JM Keller. 2007. *Recharge Data Package for Hanford Single-Shell Tank Waste Management Areas*. PNNL-16688, Pacific Northwest National Laboratory, Richland, WA.

Hammond GE, PC Lichtner, and RT Mills. 2014. "Evaluating the performance of parallel subsurface simulators: An illustrative example with PFLOTRAN." *Water Resources Research* 50(1):208-228. doi:10.1002/2012WR013483

Johnson TC, GE Hammond, and X Chen. 2017. "PFLOTRAN-E4D: A parallel open source PFLOTRAN module for simulating time-lapse electrical resistivity data." *Computers & Geosciences* 99:72-80. https://doi.org/10.1016/j.cageo.2016.09.006

Johnson TC, R Versteeg, A Ward, F Day-Lewis, and A Revil. 2010. "Improved hydrogeophysical characterization and monitoring through parallel modeling and inversion of time-domain resistivity and induced-polarization data." *Geophysics* 75(4):WA27-WA41. doi:10.1190/1.3475513

Johnson TC and D Wellman. 2013. *Re-inversion of surface electrical resistivity tomography data from the Hanford Site B-Complex*. PNNL-22520, Pacific Northwest National Laboratory, Richland, WA.

Johnson TC and D Wellman. 2015. "Accurate modelling and inversion of electrical resistivity data in the presence of metallic infrastructure with known location and dimension." *Geophysical Journal International* 202(2):1096-1108. doi:10.1093/gji/ggv206

Lesmes D and S Friedman. 2005. "Relationships between the Electrical and Hydrogeological Properties of Rocks and Soils." In: Y Rubin Y and SS Hubbard (eds), *Hydrogeophysics*. Water Science and Technology Library, vol 50. Springer, Dordrecht. pp. 87-128. https://doi.org/10.1007/1-4020-3102-5_4

Lichtner P, et al. 2015. *PFLOTRAN User Manual: A Massively Parallel Reactive Flow and Transport Model for Describing Surface and Subsurface Processes*. LA-UR-15-20403, Los Alamos National Laboratory, Los Alamos, NM.

National Fire Protection Association. 2019. *National Electrical Code 2020 Handbook*. Quincy, MA.

Niu Q and C Zhang. 2018. "Physical Explanation of Archie's Porosity Exponent in Granular Materials: A Process-Based, Pore-Scale Numerical Study." *Geophysical Research Letters* 45(4):1870-1877. https://doi.org/10.1002/2017GL076751

Nuclear Newswire. 2021. "Nevada's legacy nuclear propulsion facilities slated for demolition," September 15, 2021. *Radwaste Solutions*. https://www.ans.org/news/article-2859/leak-discovered-in-singleshell-waste-tank-at-hanford/

Oostrom M, MJ Truex, KC Carroll, and GB Chronister. 2013. "Perched-water analysis related to deep vadose zone contaminant transport and impact to groundwater." *Journal of Hydrology* 505:228-239. https://doi.org/10.1016/j.jhydrol.2013.10.001

Oostrom M, MJ Truex, ML Rockhold, and TC Johnson. 2017. "Deep Vadose Zone Contaminant Flux Evaluation at the Hanford BY-Cribs Site Using Forward and Imposed Concentration Modeling Approaches." *Environmental Processes* 4(4):771-797. doi:10.1007/s40710-017-0272-5

Robinson J, RD Mackley, ML Rockhold, TC Johnson, and P Jaysaval. 2020. G*eophysical Methods for Stratigraphic Identification*. PNNL-29182, Pacific Northwest National Laboratory, Richland, WA.

Rucker DF, et al. 2013. "Surface geophysical exploration: developing noninvasive tools to monitor past leaks around Hanford's tank farms." *Environmental Monitoring and Assessment* 185(1):995-1010. doi:10.1007/s10661-012-2609-x

Serne RJ, et al. 2010. *Conceptual Models for Migration of Key Groundwater Contaminants through the Vadose Zone and into the Upper Unconfined Aquifer below the B-complex*, PNNL-19277, Pacific Northwest National Laboratory, Richland, WA.

Singha K, FD Day-Lewis, TB Johnson, and LD Slater. 2015. "Advances in interpretation of subsurface processes with time-lapse electrical imaging." *Hydrological Processes* 29(6):1549-1576. doi:10.1002/hyp.10280

Springer SD. 2018. *Model Package Report: Central Plateau Vadose Zone Geoframework Version 1.0, Hanford Site (HNF), Richland, WA*. CP-60925, Rev. 0, CH2M Hill Plateau Remediation Company, Richland, WA. https://doi.org/10.2172/1432798

van Genuchten MT. 1980. "A Closed-form Equation for Predicting the Hydraulic Conductivity of Unsaturated Soils." *Soil Science Society of America Journal* 44(5):892-898. https://doi.org/10.2136/sssaj1980.03615995004400050002x

Yue W. 2019. "Pore-Scale Explanation of the Archie's Cementation Exponent: Microstructure, Electrical Anisotropy, and Numerical Experiments." *Geophysical Research Letters* 46:5799-5807.

Appendix A – List of Cased Wells

Table A.1. Cased wells within and surrounding the B-tank farm.[(a)]

	Well ID	X (m)	Y (m)	Bottom Elevation (m)	Depth (m)
1	299-E33-184	573880.88	137338.75	164.33	35.67
2	299-E33-185	573885.13	137326.80	169.22	30.78
3	299-E33-186	573870.13	137315.48	158.60	41.40
4	299-E33-187	573858.13	137326.83	169.31	30.69
5	299-E33-188	573865.50	137341.31	169.08	30.92
6	299-E33-183	573865.19	137310.97	169.36	30.64
7	299-E33-179	573884.94	137298.66	169.52	30.48
8	299-E33-180	573874.44	137285.94	156.94	43.06
9	299-E33-181	573864.63	137287.31	169.46	30.54
10	299-E33-182	573857.44	137298.45	169.44	30.56
11	299-E33-264	573862.63	137278.08	169.63	30.37
12	299-E33-261	573881.69	137278.39	169.57	30.43
13	299-E33-220	573886.88	137268.08	159.09	40.91
14	299-E33-262	573881.25	137255.22	169.89	30.11
15	299-E33-274	573875.44	137255.97	181.33	18.67
16	299-E33-263	573862.75	137255.17	162.55	37.45
17	299-E33-192	573833.31	137340.73	161.47	38.53
18	299-E33-189	573850.38	137338.72	169.10	30.90
19	299-E33-191	573842.19	137315.47	169.66	30.34
20	299-E33-218	573840.44	137284.17	163.35	36.65
21	299-E33-219	573854.69	137267.91	169.95	30.05
22	299-E33-221	573841.25	137252.72	159.52	40.48
23	299-E33-200	573803.63	137339.38	169.14	30.86
24	299-E33-197	573820.50	137338.02	169.21	30.79
25	299-E33-198	573811.88	137315.53	169.67	30.33
26	299-E33-54	573821.75	137309.86	148.02	51.98
27	299-E33-193	573824.44	137296.34	158.94	41.06
28	299-E33-194	573815.38	137285.75	169.77	30.23
29	299-E33-195	573800.88	137288.72	169.78	30.22
30	299-E33-196	573796.69	137298.36	154.13	45.87
31	299-E33-147	573805.31	137280.91	170.00	30.00
32	299-E33-212	573822.06	137273.92	169.88	30.12
33	299-E33-149	573816.00	137255.03	170.19	29.81
34	299-E33-148	573797.69	137262.58	159.40	40.60
35	299-E33-204	573770.38	137338.41	169.23	30.77
36	299-E33-201	573789.56	137338.44	161.55	38.45
37	299-E33-199	573795.88	137328.84	169.26	30.74

	Well ID	X (m)	Y (m)	Bottom Elevation (m)	Depth (m)
38	299-E33-202	573781.06	137315.53	169.65	30.35
39	299-E33-203	573770.38	137318.91	169.43	30.57
40	299-E33-217	573765.19	137298.16	163.65	36.35
41	299-E33-214	573779.31	137280.64	163.90	36.10
42	299-E33-213	573791.56	137273.77	169.94	30.06
43	299-E33-216	573772.81	137256.28	170.54	29.46
44	299-E33-215	573767.19	137267.81	159.64	40.36
45	299-E33-338	573912.06	137238.23	117.10	82.90
46	299-E33-47	573916.50	137295.45	123.27	76.73
47	299-E33-365	573847.63	137397.91	121.61	78.39
48	299-E33-58	573806.88	137388.06	152.92	47.08
49	299-E33-18	573779.19	137386.06	119.16	80.84
50	299-E33-190	573854.19	137326.56	169.21	30.79
51	299-E33-51	573891.13	137309.80	153.91	46.09
52	299-E33-52	573871.69	137249.42	153.67	46.33
53	299-E33-53	573852.44	137350.31	151.17	48.83
54	299-E33-55	573791.38	137350.34	151.19	48.81
55	299-E33-56	573780.13	137249.31	154.99	45.01
56	299-E33-57	573757.13	137286.69	154.61	45.39
57	299-E33-59	573797.25	137388.59	152.57	47.43
58	299-E33-60	573802.06	137379.95	152.30	47.70
59	C3103	573802.56	137385.58	130.97	69.03
60	C5163	573773.88	137227.95	181.58	18.42
61	C5167	573787.38	137232.83	184.78	15.22
62	C5169	573787.56	137228.31	184.95	15.05
63	C5161	573766.19	137224.70	187.23	12.77
64	C5165	573778.13	137240.27	184.63	15.37
65	299-E28-72	573803.38	137362.80	179.60	20.40
66	299-E33-344	573782.94	137387.31	127.56	72.44
67	299-E33-345	573780.88	137388.23	119.75	80.25
68	299-E33-46	573792.56	137278.36	119.35	80.65

(a) A top elevation of 200 m was used within the ERT simulations.

Pacific Northwest National Laboratory

902 Battelle Boulevard
P.O. Box 999
Richland, WA 99354
1-888-375-PNNL (7665)

www.pnnl.gov